Magnetic torque tweezers: measuring torsional stiffness in DNA and RecA-DNA filaments

Jan Lipfert, Jacob W J Kerssemakers, Tessa Jager & Nynke H Dekker

We introduce magnetic torque tweezers, which enable direct single-molecule measurements of torque. Our measurements of the effective torsional stiffness C of dsDNA indicated a substantial force dependence, with C = ~40 nm at low forces up to C = ~100 nm at high forces. The initial torsional stiffness of RecA filaments was nearly twofold larger than that for dsDNA, yet at moderate torques further build-up of torsional strain was prevented.

Magnetic tweezers are a powerful single-molecule technique that can be used to apply stretching forces and torques to biological molecules tethered between a surface and superparamagnetic particles[1-3]. Although forces applied in conventional magnetic tweezers can readily be calibrated[4], direct measurement of torque has proven difficult. Here we report the design of magnetic torque tweezers (MTT), which can be used to apply and directly measure both forces and torques to single biomolecules and yet have the strengths of conventional magnetic tweezers: facile application of torque, natural operation in constant force mode, straightforward extension to parallel measurements, absence of sample heating and photodamage, and simplicity and robustness.

We introduce a protocol to monitor the bead's rotation with simultaneous detection of the bead's x, y and z position, and redesigned the magnet geometry to provide an angular clamp suitable for torque measurements. In contrast to a nanorod-based approach[5], our MTT do not require complicated nanofabrication of particles, they allow for application of torque by simple rotation of the magnets and maintain the position resolution of conventional magnetic tweezers. Unlike the torque measurement schemes using a rotor bead assay[6] or an optical torque wrench[7-9], the MTT require neither lasers for fluorescence excitation, particle trapping or polarization control, nor special constructs for the tether. Our MTT cover the entire range of stretching forces relevant for studying supercoiled DNA from ~10 femtonewtons (fN) to 10 pN.

The principle of the MTT is based on the measurement of small angular deviations in a low-stiffness torsional trap (**Fig. 1a,b**). A superparamagnetic bead held in magnetic tweezers experiences a constant upward force, $\vec{F} = \vec{\nabla}(\vec{m}(\vec{B}) \cdot \vec{B})/2$, in which $\vec{B}$ is the magnetic field and the force, $\vec{F}$, is due to the magnetization, $\vec{m}$, and the gradient $\vec{\nabla}$ of the magnetic field[3,4]. The upward force exerted by the magnetic tweezers on the bead is balanced by the restoring force of the DNA tether. In addition, the bead's rotation about the z axis (along the direction of the stretched DNA) is constrained by the magnetic field. The torque exerted on the bead by the magnetic field is given by $\vec{\tau}_B = \vec{m}_0 \times \vec{B}$ in which $\vec{m}_0$ is exclusively the permanent component of the bead's magnetization[3]. Unlike the force exerted by the magnets, the torque depends on $\vec{m}_0$ (but $\vec{F}$ depends on the total magnetization, $\vec{m}$) and on the magnitude and direction of the magnetic field (but $\vec{F}$ depends on the gradient).

The stiffness of the torsional trap, k_{rot}, can be calibrated by observing the rotational thermal fluctuations $<\delta\theta^2>$ of the bead and applying the equipartition theorem

$$k_{rot} = \frac{k_B T}{\langle \delta\theta^2 \rangle} \qquad (1)$$

in which k_B is the Boltzmann constant, and T is the temperature. If the DNA tether is over- or underwound by rotating the magnets, the DNA will exert a restoring torque τ_{DNA} on the bead (**Fig. 1b**). After calibrating the trap stiffness and the equilibrium angle θ_0 of the trap for torsionally relaxed DNA, τ_{DNA} can be determined from the shift in the average angle $<\theta - \theta_0>$ away from this equilibrium[8]

$$\tau_{DNA} = -k_{rot} \langle \theta - \theta_0 \rangle \qquad (2)$$

To implement the necessary angular tracking, we attached non-magnetic, biotinylated 1.0-μm-diameter beads to streptavidin-coated 2.8-μm-diameter superparamagnetic beads that we tethered to a microscope coverslip by single DNA molecules (**Fig. 1a,c**). We analyzed slightly defocused charge-coupled device (CCD) images obtained by video microscopy (**Fig. 1d**) to track the magnetic bead's x, y and z position with a resolution of ~2–3 nm as determined from the s.d. of the traces of immobile beads (**Supplementary Fig. 1**). The smaller bead was a clear fiducial marker that allowed us to track the rotation angle simultaneously with the position of the magnetic bead (**Fig. 1d**) by considering a ring-like radial section of the bead image that was centered on the magnetic bead and included the fiducial bead (**Fig. 1e**). We used a correlation algorithm to track the fiducial bead, after unfolding the image in polar coordinates (**Fig. 1f** and **Supplementary Fig. 2**). The angular resolution of our tracking protocol was ~0.1°, as judged from angular traces of beads stuck to the surface (**Fig. 1g** and **Supplementary Figs. 3** and **4**).
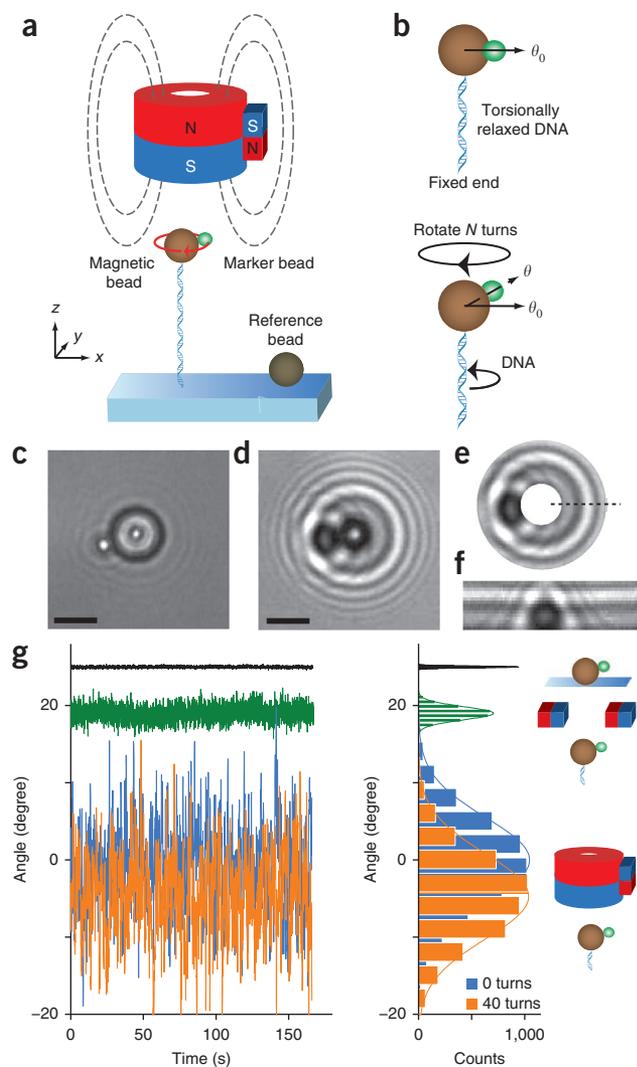
Figure 1 | Principle of magnetic torque tweezers and their operation. (**a**) The MTT setup consists of a DNA tethered magnetic bead with a smaller, nonmagnetic bead attached as a fiducial marker, a surface-attached reference bead that was used to correct for mechanical drift, a cylindrical permanent magnet to apply force and a smaller side magnet to apply torques. Magnet north and south poles are labeled N and S, respectively. (**b**) Schematic showing that after overwinding (or underwinding) the DNA tether by N turns, the DNA exerts a restoring torque on the bead that leads to a shift in the equilibrium angular position from θ_0 to θ. (**c**) CCD image of a 1.4-μm-radius magnetic bead with a 0.5-μm-radius fiducial marker in focus. Scale bar, 3 μm. (**d**) Out-of-focus image of the magnetic bead with a fiducial marker. Scale bar, 3 μm. (**e**) Radial section of the image in **d** used for angular tracking. (**f**) Transformation of the image in **e** from Cartesian (x,y) coordinates into polar (r,θ) coordinates. (**g**) Traces of rotational fluctuations obtained from analysis of CCD images for a surface-attached bead, for a DNA-tethered bead held in conventional magnetic tweezers and for a tethered bead in the MTT (each shown schematically on the right) at 0 turns (torsionally relaxed DNA), and for the same DNA after introducing 40 turns. The stretching force was 3.5 pN for all traces.

To provide MTT with sufficient sensitivity for detecting small torques, we redesigned the magnet configuration in our tweezers. In conventional magnetic tweezers, $\vec{m}_0$ is closely aligned with a horizontal magnetic field and the torsional trap stiffness k_{rot} is in the range of 10^3–10^4 pN nm rad^{-1}, which is unsuitably large for torque measurements on DNA (**Supplementary Figs. 5** and **6**). We based our MTT magnet geometry on a large cylindrical magnet aligned vertically, with the field pointing in the z direction (**Fig. 1a**), which provides a strong field gradient that pulls the magnetic bead upwards, but reduces k_{rot} by multiple orders of magnitude. For perfect alignment of the field with the z direction, we expected $\vec{m}_0$ to align in the z direction and the bead to rotate freely about the z axis, unconstrained by the magnets. Therefore, to maintain the ability to apply torques and rotate the bead, we added a small side magnet that provides a small horizontal component to the field and generates a weak angular trap with k_{rot} of ~100–500 pN nm rad^{-1} (**Supplementary Figs. 5** and **7**), allowing us to directly observe the shift in equilibrium angle induced by the torque exerted by DNA (**Fig. 1g**).

Using MTT we determined the DNA tether extension and torque response while over- and underwinding single DNA molecules (**Fig. 2** and **Supplementary Figs. 8** and **9**). Starting with a torsionally relaxed molecule at 0 turns, DNA initially behaves like an isotropic flexible rod: as positive turns are added to the molecule, its extension remains approximately constant (**Fig. 2d**) and the shift in the mean angular signal decreases linearly with increasing number of turns (**Fig. 2b,c**). The shift in the mean angle can be directly converted to torque (**Fig. 2b,c**) because the stiffness of the torsional trap is independent of the applied number of turns (**Fig. 2a**). The effective twist persistence length, C, of DNA can be determined from a fit to the torque data in the region in which the torque builds up linearly with added turns (**Fig. 2b,c**) as the torque after N turns equals $2\pi N k_B TC/L_C$, in which L_C is the contour length of DNA (we determined L_C independently; **Supplementary Fig. 10**). As we continued to apply positive turns, the build-up in torsional strain continued until a critical twist density was reached at which the molecule buckled to form plectonemic supercoils. Beyond this transition, the torque in the molecule remained constant at τ_b (**Fig. 2b,c**); additional turns led to an accumulation of plectonemic supercoils associated with a rapid decrease in extension (**Fig. 2d**). When we applied negative turns to torsionally relaxed DNA, the DNA initially behaved like an isotropic rod and exerted a restoring torque with opposite sign compared to the situation with positive turns. Under tensions of 1 pN or greater, DNA does not buckle upon further underwinding (the extension of the molecule remained approximately constant; **Fig. 2d** and **Supplementary Fig. 11**); instead the molecule denatured locally[10]. Experimentally, we measured the corresponding denaturation torque $\tau_{denat} = -10 \pm 1$ pN nm (**Fig. 2b**).

We systematically measured torque response of single DNAs to determine the buckling torque τ_b and effective twist persistence length C as a function of the stretching force F (**Fig. 2e,f**). τ_b increased systematically with increasing F (**Fig. 2e**). A simple model of DNA elasticity[11] captured the observed behavior only qualitatively, whereas a more complicated model[12] described the data quantitatively (**Fig. 2e**). At forces above 6 pN, DNA no longer formed plectonemic supercoils upon overwinding and instead underwent a transition from B- to P-DNA[6,10]. This transition occurred at 36 ± 2 pN nm (**Fig. 2e**), in agreement with published measurements (using two different methods: rotor bead assay[6] and optical torque wrench[13]).

The effective torsional stiffness of DNA depended on F: C decreased from 103 ± 5 nm at $F = 6.5$ pN to 43 ± 4 nm at $F = 0.25$ pN

Figure 2 | Torque measurements for a 7.9 kbp dsDNA molecule in PBS buffer. (**a**) The s.d. of the angular fluctuations as a function of applied turns. (**b**,**c**) The shift in the mean rotation angle as a function of applied turns and corresponding torques. (**d**) Simultaneously monitored DNA tether extension as a function of applied turns. Representative traces at indicated stretching forces are shown in **a**–**d**. (**e**) Buckling torque as a function of F determined from the plateaus in the torque versus turn data at positive turns. At 6.5 pN, the critical torque for the B-DNA to supercoiled P-DNA transition is shown (red square). Also shown are data obtained at intermediate stretching forces using optical torque tweezers[9] at low stretching forces using a magnetic nanorod probe[5] and by indirect measurements[18]. Predictions of a simple model of DNA elasticity[11] (dashed line; reduced $\chi^2 = 2.45$, $P < 0.05$) and a fit to the model by Marko[12] with the torsional stiffness of the plectonemic state determined from the fit to be $P = 25.2 \pm 2$ nm (solid line; reduced $\chi^2 = 0.74$, $P = 0.75$) are shown. (**f**) The effective twist persistence length C as a function of force determined from linear fits of the torque versus applied turns data in the elastic twist regime (MTT data). For comparison, values for C from fluorescence polarization anisotropy measurements[14–16], data obtained using a rotor bead assay[6] and indirect measurements[18] are shown. Selected points over a larger force range are shown in the inset. The line is the Moroz-Nelson model[17]. Error bars in **e** and **f** indicate s.e.m. from six to ten independent measurements.
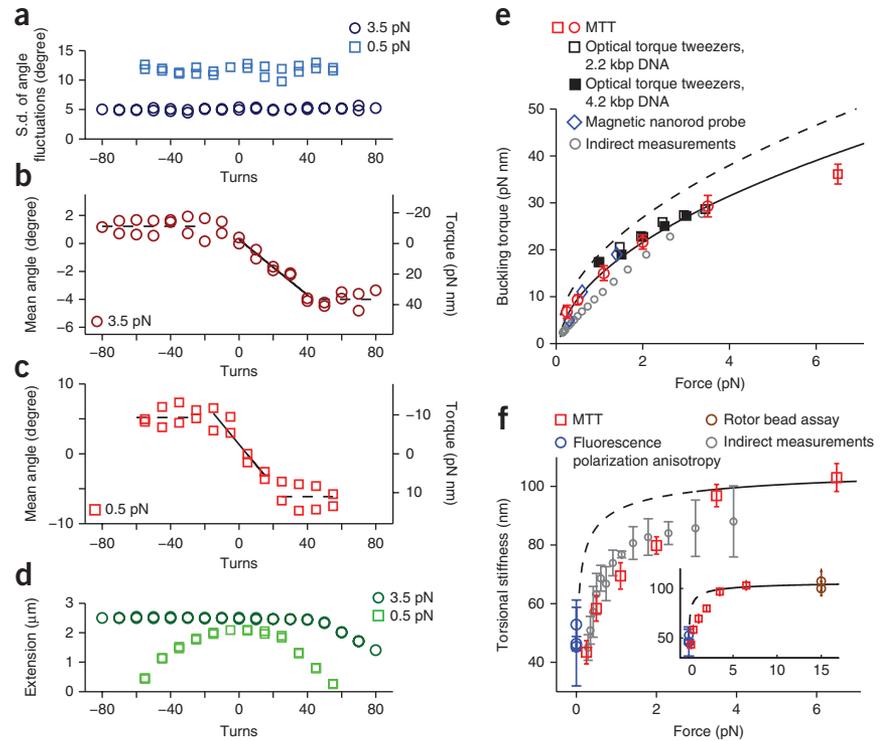

(**Fig. 2f**). The value we obtained at 6.5 pN agrees within experimental error with the values determined at forces between 15 and 45 pN (ref. 6) (**Fig. 2f**), suggesting that the force-dependence of C effectively saturates for $F \geq 6.5$ pN. Our measurement for C at 0.25 pN agreed with values determined from fluorescence polarization anisotropy measurements of short linear DNA constructs[14–16] that are effectively made at zero stretching force (**Fig. 2f**). Previous measurements with less well-defined stretching

forces and theoretical treatments that integrate data at different forces have yielded C values that were intermediate between these limits (**Supplementary Fig. 12**). Our direct measurements over the entire force range can be compared to the Moroz-Nelson[17] model for $C(F)$ and to the data obtained using an indirect approach[18] (**Fig. 2f** and **Supplementary Fig. 12**).

We also used the MTT to probe RecA filaments assembled on torsionally constrained duplex DNA in the presence of the non-hydrolyzable ATP analog ATP-γS[19,20]. In the filament one RecA monomer binds every three base pairs (bp), resulting in both stretching (0.51 nm increase in L_C per bound monomer) and unwinding ($-45°$ per bound monomer) compared to bare DNA[21] (**Fig. 3a**). RecA-dsDNA filaments had a dramatically increased bending stiffness L_P, with L_P increased at least 15-fold compared to dsDNA (**Supplementary Fig. 13**).

Upon overwinding of the torsionally relaxed filament, we initially observed an increase in the torsional strain in the molecule (**Fig. 3b** and **Supplementary Fig. 14**) and subsequently, at ~50 turns, a saturation of the torque at 39 ± 3 pN nm. The initial buildup of torque was fitted to yield $C_{RecA} = 173 \pm 5$ nm at $F = 3.5$ pN, which was 1.8-fold larger than that of bare DNA at the same force. In contrast, we observed saturation of torsional stress at a lower value of -10 ± 5 pN nm upon underwinding. Given values are means $\pm$ s.e.m. from ten independent measurements.

These measurements suggest that upon initial application of torque, torsional strain builds up in the RecA-dsDNA filament, which exhibits a higher effective torsional stiffness than dsDNA, as might have been qualitatively expected from the increased L_P and diameter of the filament. However, at torques similar to 40 pN nm upon overwinding and -10 pN nm upon underwinding, we
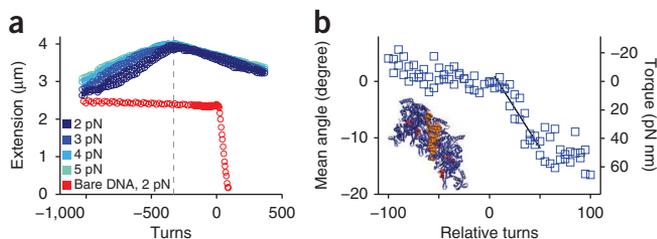
Figure 3 | Measurements of RecA-DNA heteroduplex filaments. (**a**) Rotation-extension data for RecA-dsDNA filaments at F values of 2, 3, 4 and 5 pN and for bare dsDNA at 2 pN. Dashed line indicates the center of the RecA rotation response, which was shifted to -330 turns with respect to relaxed bare DNA, as expected for full RecA coverage of our 7.9 kbp DNA construct given the observed unwinding by $-15°$ per bp upon RecA binding[21]. (**b**) Torque response of a RecA filament at $F = 3.5$ pN. Turns were measured with respect to the torsionally relaxed RecA filament (offset by +330 turns). The effective torsional stiffness was determined from a linear fit to the initial slope of the torque versus applied turns response (black line). Inset, crystallographic structure of the RecA-DNA heteroduplex filament, with RecA in blue, DNA in brown and ATP analogs bound at the RecA monomer interfaces in red (Protein Data Bank: 3CMT; ref. 21).

observed no additional build-up of torsional strain. The modest decrease in length per turn (about −1 nm per turn upon overwinding and about −1.4 nm per turn upon unwinding) suggests that the filament did not buckle. The evidence from the torque and extension measurements combined with additional experiments probing the disassembly of the filament (**Supplementary Fig. 15**) suggest that a combination of RecA unbinding and supercoiled P-DNA formation upon overwinding and DNA denaturation upon unwinding might be responsible for the observed saturation of the torsional strain.

We anticipate that MTT can be generally applied to obtain information about the material properties of biological polymers and can be a platform with which to probe protein-protein or protein-nucleic acid interactions.

METHODS

Methods and any associated references are available in the online version of the paper at http://www.nature.com/naturemethods/.

Note: Supplementary information is available on the Nature Methods website.

AUTHOR CONTRIBUTIONS

J.L., J.W.J.K. and N.H.D. designed the study, J.L. and T.J. performed the experiments, J.W.J.K. wrote the angular tracking routine and J.L. and N.H.D. wrote the manuscript.

1. Strick, T.R., Allemand, J.F., Bensimon, D., Bensimon, A. & Croquette, V. *Science* **271**, 1835–1837 (1996).
2. Bustamante, C., Bryant, Z. & Smith, S.B. *Nature* **421**, 423–427 (2003).
3. Neuman, K.C. & Nagy, A. *Nat. Methods* **5**, 491–505 (2008).
4. Lipfert, J., Hao, X. & Dekker, N.H. *Biophys. J.* **96**, 5040–5049 (2009).
5. Celedon, A. *et al. Nano Lett.* **9**, 1720–1725 (2009).
6. Bryant, Z. *et al. Nature* **424**, 338–341 (2003).
7. La Porta, A. & Wang, M.D. *Phys. Rev. Lett.* **92**, 190801 (2004).
8. Oroszi, L., Galajda, P., Kirei, H., Bottka, S. & Ormos, P. *Phys. Rev. Lett.* **97**, 058301 (2006).
9. Forth, S. *et al. Phys. Rev. Lett.* **100**, 148301 (2008).
10. Allemand, J.F., Bensimon, D., Lavery, R. & Croquette, V. *Proc. Natl. Acad. Sci. USA* **95**, 14152–14157 (1998).
11. Strick, T. *et al. Rep. Prog. Phys.* **66**, 1–45 (2003).
12. Marko, J.F. *Phys. Rev. E* **76**, 021926 (2007).
13. Sheinin, M.Y. & Wang, M.D. *Phys. Chem. Chem. Phys.* **11**, 4800–4803 (2009).
14. Fujimoto, B.S. & Schurr, J.M. *Nature* **344**, 175–177 (1990).
15. Selvin, P.R. *et al. Science* **255**, 82–85 (1992).
16. Heath, P.J., Clendenning, J.B., Fujimoto, B.S. & Schurr, J.M. *J. Mol. Biol.* **260**, 718–730 (1996).
17. Moroz, J.D. & Nelson, P. *Proc. Natl. Acad. Sci. USA* **94**, 14418–14422 (1997).
18. Mosconi, F., Allemand, J.F., Bensimon, D. & Croquette, V. *Phys. Rev. Lett.* **102**, 078301 (2009).
19. Fulconis, R. *et al. Biophys. J.* **87**, 2552–2563 (2004).
20. van der Heijden, T. *et al. Nucleic Acids Res.* **33**, 2099–2105 (2005).
21. Chen, Z., Yang, H. & Pavletich, N.P. *Nature* **453**, 489–494 (2008).

ONLINE METHODS

DNA construct. As tethers in our MTT setup, we used a 7.9-kbp DNA construct ligated at the ends to ~600-bp DNA PCR fragments that were functionalized with multiple biotin and digoxigenin groups, respectively. The 7.9-kbp DNA is the ligation product of residues 755–1153 of the pbluescrIISK plasmid (Stratagene), residues 4214–6163 and 9023–11220 of lambda-phage DNA (Promega) and residues 1945–5304 of the pSFV1 plasmid (Stratagene). The DNA tethers were attached to streptavidin-coated 2.8-μm-diameter M270 superparamagnetic beads (Invitrogen) by incubation in PBS (Sigma).

Magnetic tweezers experimental configuration. Our MTT implementation extends the capabilities of conventional magnetic tweezers[1], which have been described previously[4,22–24]. Briefly, a 100× oil-immersion objective (Olympus ACH 100X; numerical aperture (NA) = 1.25) connected to a CCD camera (Pulnix TM-6710CL) was used to image superparamagnetic beads tethered by DNA molecules to the surface of a flow cell.

Flow cells were made from glass microscope cover slips with a double layer of parafilm as a spacer. The bottom surface was coated with nitrocellulose (0.01% (wt/vol) in amyl acetate) and flow cells were stored dry. Before measurements, 3.0-μm-diameter nonmagnetic latex beads (Invitrogen) were unspecifically attached to the bottom surface by incubation in PBS for 30 min to act as reference beads. Before addition of the DNA-linked magnetic beads, the bottom surface was functionalized by incubation with 100 μg ml^{-1} anti-digoxigenin (Roche) in PBS for 30 min to provide for DNA attachment and was passivated by incubating for 30 min with 2 mg ml^{-1} bovine serum albumin (Sigma). The positions of a DNA-tethered bead and a reference bead attached to the surface were tracked simultaneously at a rate of up to 120 Hz. From analysis of the CCD images, the bead positions in x, y and z dimensions were determined (see below).

After subtraction of the reference bead position to correct for mechanical drift, the tethered bead was tracked with an accuracy of < 5 nm in x, y and z dimensions (**Supplementary Fig. 1**). From analysis of the bead's fluctuations, the stretching force applied to the tethered bead (the magnetic force pulls the bead away from the surface) was computed[1,25,26].

Magnets for MTT. To apply forces and torques, we placed magnets with a center opening for LED illumination above the flow cell. The main magnet was a cylindrical magnet formed by a stack of three magnets (R-06-02-02-G, Supermagnete) for a total height of 6 mm, with a diameter of 6 mm and a 2-mm-diameter central aperture. An additional magnet (S-04-07-N, Supermagnete) was added on one side of the cylindrical magnet to allow for the application of torque. The side magnet had the shape of a solid cylinder, with 4-mm diameter and a height of 7 mm. A detailed schematic of the magnet assembly is presented in **Supplementary Figure 16**.

Rotational tracking by video microscopy. After tethering the magnetic beads to the surface, we specifically attached smaller, nonmagnetic beads to act as fiducial markers for tracking the magnetic beads' rotation. As fiducials, we used biotin-labeled 1.0-μm-diameter Fluosphere microspheres (Invitrogen). Incubation of the flow cell with 1,000-fold diluted Fluosphere beads for 30–60 min

lead to attachment of typically one or more marker beads per tethered magnetic bead. The 1.0-μm-diameter marker beads provided sufficient asymmetry of the bead image to track the rotation angle via cross-correlation analysis of the CCD images with an accuracy of ~0.1° (**Fig. 1g** and **Supplementary Fig. 4a**) using the following algorithm.

The defocused microscope image of a magnetic bead with a smaller, nonmagnetic fiducial bead attached was still nearly circularly symmetric but contained a small protrusion on one side (**Fig. 1d** and **Supplementary Fig. 2a**). As most of the ring pattern is unaffected, the x-y–tracking procedure by cross-correlation analysis[25] still closely approximated the symmetry center of the main bead and we achieved an accuracy of 2–3 nm as judged by the s.d. of traces recorded with surface attached beads (**Supplementary Fig. 1**). For tracking the relative angle of the protrusion, a polar coordinate grid $[r, \phi]$ grid was defined using the center position determined from the x-y tracking as the coordinate center. The range of the angular coordinate ϕ is 360 degrees and comprises 360 p_d steps, with p_d being the number of points per degree. The radial coordinate, r, runs from minimum to maximum values r_{min} to r_{max} with increments of p_r per pixel unit. The truncated image that results using a typical choice of r_{min} and r_{max} is shown in **Supplementary Figure 2b**. Using these coordinates, we generated an image in polar coordinates $P(r, \phi)$ (**Supplementary Fig. 2c**) using interpolated pixel intensities $S(i', j')$ from the original image, in which i' and j' are noninteger pixel coordinates:

$$i' = i + \delta_i = r\sin(\phi) \quad \text{and} \quad j' = j + \delta_j = r\cos(\phi) \qquad (3)$$

in which i and j are the truncated integer values, and $\delta_{i,j}$ is the difference between the fractional pixel coordinate and its truncated integer value. To track the rotation of the bead, which corresponds to pattern changes along the ϕ direction, we summed the polar map over r:

$$P(\phi) = \sum_{r_{min}}^{r_{max}} P(r, \phi) \qquad (4)$$

The resulting curve produced an angular signature of the bead and shifted proportionally and periodically with ϕ when the bead and its corresponding image pattern rotated. To quantify the relative change in ϕ, we performed a cross-correlation of $P(\phi)$ with its own mirror function $P(-\phi)$ (**Supplementary Fig. 2d**). To speed up the numerical calculation of this cross-correlation, it was performed via the respective fast Fourier transforms (FFT):

$$C(\phi) = \text{FFT}^{-1}\big(\text{FFT}(P(\phi)) \times \text{FFT}(P(-\phi))\big) \qquad (5)$$

The correlation function of the angular signatures (**Supplementary Fig. 2e**) exhibited a maximum that shifted twice as fast as a corresponding rotation (which caused the tracked angles to have a periodicity π). To achieve a resolution of less than one angular bin (of $1/p_d$ of a degree), a subpixel fitting step was performed by selecting a five-point subsection around the maximum (**Supplementary Fig. 2f**). This subsection was subjected to a parabolic fit, and the subpixel location of the maximum of the fit was scaled with $p_d/2$ to yield a relative angle. Unwrapping of the angle was performed a posteriori in the angular trace by detecting sudden changes in the signal close to π. Such phase jumps were compensated for by adding a phase shift of π to all the signal values after the jump. Our implementation

of this tracking algorithm in Labview 2009 (National Instruments) is available as **Supplementary Software**.

Buffer conditions and RecA stocks. Experiments on bare DNA were carried out in PBS (137 mM NaCl, 2.7 mM KCl and 10 mM phosphate (pH 7.4); Sigma) supplemented with 100 μg ml⁻¹ BSA (Sigma), 0.1% Tween (Sigma) and 5 mM sodium azide (Sigma). RecA experiments were performed in a buffer of similar ionic strength, namely 20 mM MES (2-(N-morpholino)ethanesulfonic acid) buffer (Sigma), pH 6.2, with 1 mM MgCl₂ (Sigma), 50 mM NaCl (Sigma), 1 mM DTT (dithiothreitol; Sigma) and 0.1 mM ATP-γS (Roche Diagnostics). We used commercially available RecA stock (New England Biolabs) at a final concentration of 5 μM.

Estimate of the torque measurement error. We estimated the error of our torque measurement from basic considerations of error propagation and Brownian fluctuations. The torque measurement in the MTT was achieved from a measurement of the shift of the mean angle from its equilibrium value (equation (2)) after calibrating the trap stiffness k_{rot}. The error in the torque measurement σ_τ was approximately given by

$$\sigma_\tau = k_{rot}\sigma_\theta \tag{6}$$

in which σ_θ is the error in the determination of the angular deflection and k_{rot} the stiffness of the torsional trap. The measurement of the mean angle had two sources of measurement uncertainty: one kind of error, σ_{BM}, stems from the fact that the particle was undergoing (rotational) Brownian motion and experienced thermal fluctuations; the second type of error, σ_{meas}, stemmed from errors in the measurement, such as inaccuracies of the tracker, drifts of the flow cell, small changes in the illumination, inaccuracies of the magnet positioning and other sources of experimental error. As these two sources of error are approximately independent, they add in quadrature

$$\sigma_\theta = \sqrt{\sigma_{BM}^2 + \sigma_{meas}^2} \tag{7}$$

The magnitude of the error owing to Brownian motion of the particle can be estimated as follows. The particle undergoes fluctuations with a width $\delta\theta$ given by the stiffness of the trap, by rearranging equation (1)

$$\langle \delta\theta^2 \rangle = \frac{k_B T}{k_{rot}} \tag{8}$$

The effect of the Brownian fluctuations can be averaged out by measuring the rotation angle over a time period t_{meas}. The resulting estimate, which is essentially the s.e.m., will have an uncertainty given by $\delta\theta/(N(\tau_C))^{1/2}$, where $N(\tau_C)$ is the number of independent measurements, spaced by approximately one characteristic time τ_C of the system, that is, $N(\tau_C) = t_{meas}/\tau_C$.

The characteristic time τ_C was determined by the rotational friction coefficient γ and the trap stiffness: $\tau_C = \gamma/k_{rot}$ (**Supplementary Fig. 7**). Combining the expression for $N(\tau_C)$ with equation (8), we find

$$\sigma_{BM}^2 = \frac{k_B T}{k_{rot}} \frac{\tau_C}{t_{meas}} = \frac{k_B T\gamma}{k_{rot}^2 t_{meas}} \tag{9}$$

This expression is analogous to the thermal limit of position detection[27].

Limit $\sigma_{BM} \gg \sigma_{meas}$. If we consider a 'perfect' measurement in which the intrinsic measurement error is zero, that is, $\sigma_{meas} = 0$, the accuracy of the torque measurement will be limited by Brownian motion alone. More realistically, we consider the case in which the Brownian motion error dominates the overall error, which will be the case for weak traps and short measurements, that is, when k_{rot} and t_{meas} are small. In this limit, the error on the torque measurement simplifies to

$$\sigma_\tau \approx k_{rot}\sigma_{BM} = \sqrt{\frac{k_B T\gamma}{t_{meas}}} \tag{10}$$

We note that in the limit in which σ_{meas} is negligible, the accuracy of the torque measurement is independent of the trap stiffness: a softer trap leads to a smaller torque error for a given level of accuracy in the angle determination, but to achieve a given accuracy in angle, we have to integrate much longer with the softer trap. Overall, the two effects cancel and the factor k_{rot} drops out of the expression for σ_τ. For our system, the rotational friction coefficient γ was 100–200 pN nm s (**Supplementary Fig. 7**). Using $k_B T = 4.1$ pN nm and $\gamma = 150$ pN nm s, equation (10) implies an error of ~10 pN nm for a $t_{meas} = 6$ s measurement and an error of 1 pN nm for a $t_{meas} = 600$ s measurement from Brownian motion alone.

Limit $\sigma_{BM} \ll \sigma_{meas}$. For any real measurement, there will be a contribution to the error on the torque measurement from measurement uncertainties because of tracker error, drift of the instrument and illumination, among others, which are summarized in σ_{meas}. It is instructive to consider the limit in which σ_{meas} dominates, that is, the limit of negligible Brownian motion. In this limit, the error in torque for a given measurement error σ_{meas} is directly proportional to k_{rot}. This is the reason why we redesigned the magnet geometry for the MTT to substantially lower the trap stiffness. An instrument error of $\sigma_{meas} = 0.1°$ corresponds to an error in the torque measurement of < 1 pN nm for trap stiffnesses in the range of 100–500 pN nm rad⁻¹ (**Supplementary Fig. 5b**), which is acceptable if measuring DNA in which the characteristic torques are on the order of ~ 10 pN nm. In contrast, in conventional magnetic tweezers, the torque trap has a stiffness of 10³–10⁴ pN nm rad⁻¹ (**Supplementary Fig. 5b**), corresponding to a torque error of 18–180 pN nm, which makes systematic measurement of DNA unfeasible (**Supplementary Fig. 6b**).

In practice, in our instrument $\sigma_{meas} = 0.1$–$0.2°$ (**Fig. 1g**, **Supplementary Figs. 4a** and **6**), and we measured each torque value, that is, each plateau in the twist curve, for typically $t_{meas} = 300$ s. In this regime, both σ_{BM} and σ_{meas} contributed to the total torque error, which was ~1–3 pN nm from measurement to measurement.

22. Koster, D.A., Croquette, V., Dekker, C., Shuman, S. & Dekker, N.H. *Nature* **434**, 671–674 (2005).
23. Crut, A., Nair, P.A., Koster, D.A., Shuman, S. & Dekker, N.H. *Proc. Natl. Acad. Sci. USA* **105**, 6894–6899 (2008).
24. Lipfert, J., Koster, D.A., Vilfan, I.D., Hage, S. & Dekker, N.H. *Methods Mol. Biol.* **582**, 71–89 (2009).
25. Gosse, C. & Croquette, V. *Biophys. J.* **82**, 3314–3329 (2002).
26. te Velthuis, A.J., Kerssemakers, J.W., Lipfert, J. & Dekker, N.H. *Biophys. J.* **99**, 1292–1302 (2010).
27. Czerwinski, F., Richardson, A.C. & Oddershede, L.B. *Opt. Express* **17**, 13255–13269 (2009).